AEROSOL INFLUENCE ON CLOUD MICROPHYSICS EXAMINED BY SATELLITE MEASUREMENTS AND CHEMICAL TRANSPORT MODELING

Harshvardhan[1], S. E. Schwartz[2], C. M. Benkovitz[2], G. Guo[1]

Revised June 2001

[1] Dept. of Earth & Atmospheric Sciences, Purdue University, West Lafayette, Indiana

[2] Atmospheric Sciences Division, Brookhaven National Laboratory, Upton, New York

Corresponding author address: Dr. Harshvardhan, Dept. of Earth and Atmospheric Sciences, Purdue University, West Lafayette, IN 47907-1397

Email: harsh@purdue.edu

ABSTRACT

Anthropogenic aerosols are hypothesized to decrease cloud drop radius and increase cloud droplet number concentration enhancing cloud optical depth and albedo. Here we have used results from a chemical transport model driven by the output of a numerical weather prediction model to identify an incursion of sulfate-laden air from the European continent over mid North Atlantic under the influence of a cut-off low-pressure system during 2-8 April 1987. Advanced Very High Resolution Radiometer (AVHRR) measurements of visible and near-infrared radiance are used to infer microphysical properties of low-altitude (T = 260-275 K) maritime clouds over the course of the event. Examination of the cloud optical depth, drop radius, and drop number concentration on the high- and low-sulfate days has allowed identification of the increase in cloud droplet number concentration and decrease in cloud drop radius associated with the sulfate incursion. These observations are consistent with the Twomey mechanism of indirect radiative forcing of climate by aerosols.

1. Introduction

It is now generally accepted that a complete picture of anthropogenic radiative forcing of the earth system requires consideration of aerosols (Haywood and Boucher 2000). Three classes of aerosol radiative forcing may be distinguished. Direct forcing is an increase (usually) in system albedo caused by the additional atmospheric optical depth in cloud-free sky. Indirect forcing arises from an increase of cloud droplet number concentration, leading to (i) an increase in system albedo (Twomey 1977) and (ii) inhibition of drizzle and resultant increase of cloud liquid water path and lifetime (Albrecht 1989). Additionally, reduction in cloud cover caused by solar absorption in haze layers (Hansen et al. 1997; Ackerman et al. 2000) may be considered a "semi-direct" effect. These forcings together are potentially of magnitude comparable to greenhouse gas forcing (Shine et al. 1995; Haywood and Boucher 2000) and in the aggregate are thought to be negative; i.e., they exert a cooling influence opposite to the direction of greenhouse gas forcing. Although the magnitudes of both direct and indirect aerosol radiative forcings on a global scale are quite uncertain, study of the various kinds of indirect radiative forcing is particularly problematic because they involve subtle changes in cloud radiative properties and lifetimes.

With respect to the classic Twomey effect, numerous *in-situ* studies have demonstrated the enhancement of cloud droplet concentrations by anthropogenic aerosols (Schwartz and Slingo 1996). Studies relating the enhancement of cloud droplet concentrations to enhanced cloud albedo have typically been limited to *in-situ* and remotely sensed characterization of cloud microphysics during intensive field campaigns, such as the FIRE ship track study of Radke et al. (1989) and the comparison of pristine maritime air and continental air influenced by industrial emissions during ASTEX (Albrecht et al. 1995) and ACE-2 (Brenguier et al. 2000). Global satellite surveys have shown differences in mean cloud microphysical properties between continental and maritime clouds and also inter-hemispheric differences (Han et al. 1994, 1998). Although cloud processes are best studied by *in-situ* investigations, these are prohibitively expensive to conduct on anything close to a global scale. The standard solution to this dilemma is to resort to remote sensing procedures anchored by limited *in-situ* results. Unfortunately,

aerosols cannot be detected remotely in the presence of cloud, although nearby clear regions can provide some estimate of the aerosol influencing the cloud microphysical properties (Wetzel and Stowe 1999).

Here we investigate the effect of aerosol on low-level clouds in a synoptic framework by a hybrid method. We use the sulfate column burden simulated by a chemical transport and transformation model as an indicator of aerosol concentration. Cloud microphysical properties are inferred remotely with data from the satellite-borne Advanced Very High Resolution Radiometer (AVHRR). Information from the two sources is combined to assess the potential of aerosol indirect radiative forcing. This approach takes explicit advantage of the large temporal variability that characterizes aerosol loading to identify a situation for which there may be a strong signal of indirect aerosol effect in cloud properties observable by satellite measurements.

2. Chemical Transport Model

The model used for the study is the Brookhaven National Laboratory (BNL) chemical transport and transformation model, the **G**lobal **Ch**emistry **M**odel driven by **O**bservation-derived synoptic meteorological data (GChM-O), which is described in Benkovitz et al. (1994) and Benkovitz and Schwartz (1997), wherein the results of extensive comparison of the sulfate mixing ratio in the lowest model layer with data from monitoring networks are also provided. The model is a three-dimensional Eulerian transport and transformation model driven by the first guess data from the forecast model of the European Centre for Medium Range Weather Forecasts (ECMWF). The model represents emissions of the several sulfur species, chemical conversion of SO_2 to sulfate by H_2O_2 and O_3 in the aqueous phase and by OH in the gas phase, chemical conversion of DMS to SO_2 and MSA by OH, and removal by wet and dry deposition. The model tracks the several sulfur species according to the source type and region and conversion mechanism. It has a horizontal grid spacing of 1.125° latitude × 1.125° longitude, 15 levels to 100 hPa and outputs the mixing ratios of SO_2 and sulfate at each grid cell location and model level at 6-hour time intervals.

Output of a model run for April 1987 was used to identify a time period and region for investigating the indirect radiative effect of anthropogenic aerosols in the North Atlantic. During early April the eastern North Atlantic came under the influence of a cut-off low-pressure system that transported boundary layer air from source regions in northwestern Europe. The meteorological conditions leading to the high sulfate column burden (vertical integral of concentration) in this region have been discussed in some detail by Benkovitz et al. (2001a,b). Figures 1 and 2 show respectively, visible and infrared NOAA-9 AVHRR images of the region for the period 2 - 8 April 1987. Note the extensive low-level clouds, including the classic display of open cellular convection typical of the passage of cold air over warmer water (Agee 1987; Bader et al. 1995). On 3 April a high-amplitude trough developed at 500 hPa off western Europe with an associated strong surface storm at 925 hPa. A broad area of high SO_2 burden extended through northern Europe across the North Sea and into the Atlantic just north of the United Kingdom. This high-amplitude trough evolved from 3 April to 5 April into an intense cut-off low, which exhibited concentric circulation on all isentropic surfaces with little slantwise transport into or out of the core of the disturbance. During this period the air mass from over the European continent was recirculated by the developing cut-off low, with SO_2 being oxidized to produce a sulfate column burden of several hundred μmol m^{-2} on the southern part of the low by 0000 UTC 5 April. Large values of sulfate column burden persisted in the region for more than 72 hours.

We focus here on the period 2-8 April and the area bounded by latitudes 50N and 55N and longitudes 25W and 30W to investigate changes in cloud microphysics over the time period. As we wish to examine the relation between cloud microphysical properties and the intrusion of sulfate aerosol from Europe it is necessary to minimize other sources of aerosol such as desert dust or organics from biomass burning. Restricting the analysis to the higher latitudes reduces the possibility of contamination, although it probably does not eliminate it altogether. Figure 3 shows the vertical profile of sulfate concentration averaged over 50-55N and 25-30W as simulated by GChM-O at 1200 UTC on the dates marked. The enhancement is confined mainly

to the lowest two to three kilometers of the atmosphere, coincident with the typical extent of the low-level clouds as discussed later. The sulfate derives almost entirely from European sources, consistent with the circulation, with substantial contributions from both gas-phase and aqueous-phase oxidation of SO_2 and substantially less primary sulfate (Benkovitz et al. 2001b).

3. Remotely Sensed Data

a. Methodology

For this study we have obtained cloud microphysical information from a two-channel method using AVHRR Global Area Coverage (GAC) data (Nakajima and Nakajima 1995). The procedure makes use of Channels 1 (visible, 0.58–0.68 μm) and 3 (near-infrared, 3.55–3.93 μm) to obtain cloud droplet effective radius, r_e, and cloud optical depth at 0.64 μm, τ_c, for each pixel. The effective radius used throughout follows the definition of Hansen and Travis (1974), $r_e = \mu_3 / \mu_2$, where μ_i denotes the *i*th moment of the cloud droplet size distribution, i.e.

$$\mu_i = \int r^i \, n\,(r)\, dr, \tag{1}$$

where $n\,(r)\,dr$ is the number concentration of cloud droplets in the radius interval r to $r + dr$. The theoretical basis of such retrievals is discussed by Nakajima and King (1990). Briefly, use is made of the fact that the reflectance of absorbing cloud layers at wavelengths in the water vapor window spectral regions of the solar near-infrared asymptotes at high cloud optical depth to a value determined primarily by the single scattering albedo of the cloud droplets (King 1987). Furthermore, the co-albedo, a measure of droplet absorption, is linearly related to the radius of the droplets (Twomey and Bohren 1980). The net result is that the reflectance in AVHRR Channel 3, which encompasses a spectral region of fairly substantial droplet absorption, can be related to the effective radius of the droplets making up the cloud layer (Platnick and Valero 1995). AVHRR Channel 1, which is in the visible portion of the solar spectrum, where water droplets do not appreciably absorb (barring absorbing impurities), provides information on the optical thickness of the cloud because, for conservative scattering, the reflectance increases monotonically with increasing optical depth (King 1987). Retrieval methods using Channels 1

and 3 of AVHRR have the additional benefit relative to methods using shorter wavelengths in the near-infrared (Brenguier et al. 2000) that isolines of reflected radiances in the two channels are nearly orthogonal so long as $\tau_c > 4$ and $r_e > 4\mu m$ (Nakajima and Nakajima 1995).

Retrieval methods using AVHRR Channel 3 are subject to interference from thermal emission from the surface and cloud tops that is comparable to the reflected radiance; the measured radiance is the sum of these two contributions. Several techniques have been used to remove the thermal emission contribution; here we use the technique of Kaufman and Nakajima (1993), who used the effective radiating temperature of the scene obtained from Channel 4 (infrared, 10.3–11.3 μm) and the optical depth obtained from Channel 1 to remove the emission contribution to Channel 3 radiances. The technique needs information on surface temperature in addition to the standard atmospheric conditions assumed in the retrieval process; we use sea surface temperature data from the compilation of Reynolds (1988). AVHRR pixel counts in Channel 1 have been adjusted for sensor degradation following Kaufman and Holben (1993). The lookup tables created for the inversion procedure assumed a standard mid-latitude summer atmosphere and surface albedo of 0.02. Retrievals are not made when the inferred optical depth exceeds 70.0 or the effective radius exceeds 30.0 μm.

b. Spatial Coherence Screening

As the inversion process is based on one-dimensional plane-parallel radiative transfer, caution must be used in selecting pixels for processing and interpreting results. For this study, we have restricted ourselves to oceanic regions, so the background albedo is low and homogeneous. Furthermore, we have used a lower cutoff of 10% in Channel 1 reflectance to eliminate pixels that could be covered by haze but not clouds and a 250K cutoff in Channel 4 radiating temperature to eliminate high clouds. GAC pixels are roughly 4×1 km at nadir, and hence there is a good chance that they are not completely covered by clouds. Partially filled pixels will bias the inferred retrievals of effective radius and optical depth. One way around this problem would be to use a higher threshold for the visible channel, which should eliminate most partially filled pixels. However, this also eliminates many cloud-covered pixels for which

information should be included and restricts the analysis to the thicker portions of the cloud field. The screening procedure is illustrated in Figures 4 and 5 for the data of 2 April 1987. Figure 4a is a scatter plot of Channel 1 reflectance versus Channel 4 radiating temperature for all GAC pixels in the study area on 2 April 1987. There is a continuum of reflectance values and no obvious choice for a threshold. In this study we have opted for the screening technique pioneered by Coakley and Bretherton (1982) – the spatial coherence method, which has been applied to GAC data (Coakley and Davies 1986). We use the local standard deviation of Channel 4 radiance in 2 $\times$ 2 pixel arrays to screen out partially cloud-filled pixels. Figure 4b is a scatter plot of Channel 4 local standard deviation in radiance units plotted versus Channel 4 radiating temperature for 2×2 arrays of all the pixels in Fig. 4a. The clusters of points identified by small values of the local standard deviation at the cold and warm ends of the arch represent, respectively, cloud tops and the ocean surface. These pixels are relatively uniform in radiating temperature at the scale of four adjacent GAC pixels, roughly 50 km^2 at nadir.

Figure 5a shows the retrieved cloud optical depth and corresponding inferred cloud top temperature for all pixels in Fig. 4a having Channel 1 reflectance in excess of 10% and Channel 4 radiating temperature greater than 250K while Fig. 5b shows the subset that are contained in $2 \times$ 2 pixel arrays having Channel 4 local standard deviation less than 0.5 mW m^{-2} sr^{-1} cm. The inferred cloud top temperatures are typically colder than the Channel 4 radiating temperatures shown in Fig. 3b because the contribution to radiance resulting from transmission of underlying surface emission has been taken into account. The sharp cutoff at an optical depth of about 3 is a result of the Channel 1 reflectance threshold of 10%. Application of the standard deviation threshold eliminates the numerous pixels that are almost certainly partially cloud filled. These pixels have low Channel 1 reflectance and warm Channel 4 radiating temperatures but are probably not extensive thin, low clouds. Restricting the analysis to pixels passing the standard deviation criterion allows inclusion of a full range of retrieved optical depths and effective droplet radii for cloud-filled pixels while at the same time reducing biases that would appear if all pixels were analyzed. Han et al. (1994) estimate that the overcast assumption for partly cloud filled

pixels introduces a bias of 10% in optical depth and 1 μm in effective radius, but Loeb and Coakley (1998) show that these biases could be much larger, especially for measurements made in the forward scattering direction. We have attempted to reduce these biases but cannot eliminate them completely because pixels still exhibit optical and geometric inhomogeneity at the GAC pixel scale (Cahalan et al.1994).

c. Retrieval Errors

There are other errors associated with the inversion technique resulting from the assumption of a vertically uniform profile of the effective radius with height and of climatological vapor and temperature profiles. Nakajima et al. (1991) found that the procedure used here underestimates r_e at cloud top by roughly 10% when compared to a model cloud in which r_e increases linearly with height. In addition, τ was overestimated by 1-5%. There is also an uncertainty of 1-3% in both τ and r_e resulting from the assumption of a fixed standard water vapor profile. The assumption of a low uniform surface albedo has negligible effect on the retrieved optical depth of optically thick clouds and no effect at all on retrieved drop size (Nakajima and Nakajima, 1995).

Cloud tops in the current analysis are colder than 273K and it is possible that some of the pixels contain clouds that are glaciated. The retrieval assumes spherical water drops. The main effect of this misclassification would be the retrieval of significantly larger drop sizes, most probably in excess of the 30 μm limit used here. For each scene 1-2% of all pixels were rejected based on this effective radius criterion. However, there is no certainty that all the pixels included in the analysis are filled with clouds consisting only of water drops.

4. Cloud microphysics

The effective radius, r_e, inferred from the inversion of the satellite data is a measure of the droplet size at some distance just below the top of the cloud, averaged horizontally over the entire pixel (Nakajima and King 1990). The optical depth, τ_c, is also a radiance-weighted measure representative of the pixel. An additional key microphysical quantity, the column droplet

concentration, C (cm^{-2}), which is the vertical integral of the cloud droplet number concentration, N (cm^{-3}), is derived from r_e and τ_c in the following manner. The liquid water path, W ($g\ m^{-2}$), the integral of the condensed water content in a vertical column extending from the base to the top of the cloud, is approximated by (Stephens 1984)

$$W = \frac{2\rho_w \tau_c \langle r_e \rangle}{3}. \tag{2}$$

From (2) we compute the column droplet concentration, C (cm^{-2}), following Han et al. (1998):

$$C = \frac{3W}{4\pi\rho_w \langle r_e^3 \rangle k}. \tag{3}$$

In the above, angle brackets denote a vertical average through the cloud, ρ_w is the density of liquid water and the factor k given by

$$k = \frac{\mu_2^3}{\mu_0 \mu_3^2}, \tag{4}$$

is determined by the shape of the drop size distribution and has a value near unity. For a monodisperse distribution k=1, the value of k decreases as the distribution broadens. Martin et al. (1994) reported results from extensive measurements in maritime and continental air masses. They cite values of $k = 0.67 \pm 0.07$ for continental air masses and $k = 0.80 \pm 0.07$ for maritime cases; here we choose $k = 0.735$, which is the midpoint of the range realizing full well that there may have been variations in this factor over the study period. As the reflected radiance measured remotely does not provide information from deeper regions of the cloud, some assumptions need to be made in order to infer the column-mean effective radius from the cloud-top effective radius, r_e.

Han et al. (1998) realized that using r_e at cloud top would be a 20-35% overestimate and adjusted the value of k accordingly. Brenguier et al. (2000) showed that the relationship $\langle r_e \rangle = 5/6\ r_e$ should be expected when comparing a vertically uniform and adiabatically stratified model having the same optical depth and liquid water path. However, their radiative transfer simulations show departures from this relationship. Here we assume that the size distribution at

the level where the effective radius is 5/6 of the value at cloud top is representative of the vertical column and apply the factor *k* at that level in eq. (3).

5. Results and discussion

Table 1 summarizes the solar illumination and satellite viewing geometry of the study area during the period of the analysis. During the period 3-5 April, the study area, encompassed by latitudes 50N-55N and longitudes 25-30W, was close to the sub-satellite track. The solar zenith angle throughout the entire period varied only slightly, between 50° and 60°. On 8 April, retrievals were made for two overpasses, one in the forward scattering direction and roughly 100 minutes later, in the backscattering direction. We thus have eight separate cases for the retrieval of cloud properties. The table also lists the sulfate column burden simulated by the BNL GChM-O during the study period. The values cited are averages over all the model grid points falling within the study area. To recap what was mentioned in Section 2, there was a substantial intrusion of industrially influenced air into the area at low levels starting around 4 April, and sulfate levels remained elevated for the next three days. Finally, the table presents our estimates of the cloud base, cloud top and cloud droplet number concentration obtained from the analysis. The manner in which these were obtained is explained following the presentation of the directly retrieved cloud properties.

Figure 6 shows the retrieved effective radii plotted versus cloud top temperature for the eight cases. Pixels at the colder limit of the clusters represent the highest cloud tops in the region. A portion of the vertical spread shown in the panels simply reflects the roughly 3° C gradient in SST across the 5° of latitude, which would be mirrored in a corresponding gradient of temperature at cloud top. However, the temperature range on most days is well in excess of that, and we are almost certainly seeing cloud elements that have grown to different elevations from a common cloud base level. The panels for 2,3 and 8 April, before and after the sulfate incursion show similar cloud microphysical properties. The lowest cloud tops have effective radii of about 8 μm and the drop size increases with increasing altitude (decreasing temperature) to values in

excess of 20 μm. This is consistent with droplet growth mechanisms in maritime boundary layer clouds (Brenguier et al. 2000) and tropical convective clouds (Rosenfeld and Lensky 1998) having low concentrations of cloud condensation nuclei (CCN). The situation from 4 – 7 April is quite different. The droplet radii are much smaller and their growth is limited such that the radius range does not exhibit evident dependence on cloud top height, a characteristic observed by Brenguier et al. (2000) in boundary-layer stratus clouds under polluted conditions.

Figure 7 examines the relationship between cloud droplet radius and optical depth. On all days, the smallest droplets are associated with the thinnest clouds and with droplet sizes tending to increase with increasing optical depth. This is consistent with the observational studies of Nakajima et al. (1991), Han et al. (1994) and Nakajima and Nakajima (1995) and the modeling study of Lohmann et al. (2000). Those investigators also reported a decrease in drop radius with increasing optical depth for thicker clouds ($\tau_c > 20$). However, there is no indication of such a trend in the present data, with the possible exception of the 2 April case. Nakajima et al. (1991) attribute the negative correlation to the presence of drizzle in deeper clouds, and Lohmann et al. (2000) have been able to simulate such a negative correlation resulting from precipitation processes in a general circulation model. The 4 – 7 April results show that droplet sizes are constrained from growing beyond about 12 μm on the days with high sulfate loading. Perhaps droplet growth is being suppressed because of competition for the limited amount of condensed water available and droplets are unable to grow sufficiently large for drizzle initiation. Finally, the decrease in effective radius as the sulfate concentration increases (2 – 5 April) and the recovery toward the end of the episode (6 – 8 April) are particularly evident in this figure.

The increased availability of CCN on high-sulfate days also manifests itself in an increase in cloud droplet concentration. Figure 8 shows scatter plots of the column-integrated cloud drop concentration, *C*, given by (3) versus the cloud top temperature. These plots show relatively low column droplet concentration before the incursion of sulfate into the region. There is a three- to four-fold increase on 4 and 5 April followed by a return to much lower values on 8 April. This behavior is consistent with the enhancement of cloud drop number concentration due to the

sulfate aerosol, but the column concentration by itself does not provide a measure of the cloud droplet number concentration without knowledge of the vertical extent.

To examine the relation between cloud drop concentration and sulfate we use an adiabatic model (Brenguier et al. 2000) to infer cloud drop concentration. If air parcels ascend without mixing with dry air from outside or above the cloud, the number concentration of droplets will be constant through the cloud although the droplets themselves will continue to increase in size. The column concentration will then increase linearly with height above cloud base. As we do not have direct knowledge of the base, we have inferred the lifting condensation level from meteorological analysis at 1200 UTC at the center of the region under study. Temperature and relative humidity at 1000 mb in the analyses described by Trenberth (1992) are used to estimate the lifting condensation level. An estimate of the cloud top temperature representative of the entire grid box is the mid-point of the scatter shown in each panel of Figures 6 and 8. The cloud top altitude is estimated assuming a moist adiabatic lapse rate of 6.5 K km^{-1} from the cloud base.

We now assume that the largest values of C at each temperature level of the scatter plots in Figure 8 represent parcels that have undergone adiabatic ascent and that smaller values at each level represent parcels that have mixed with clear air, diluting the number concentration (Brenguier et al. 2000). The straight lines drawn on the panels in Figure 8 represent adiabatic ascent from the cloud base. They are necessarily drawn in a subjective manner; the slope gives an estimate of the corresponding value of adiabatic droplet number concentration, N_{ad}, which is also listed in Table 1. The values inferred on the high- and low-sulfate days are consistent with measurements made during ASTEX (Albrecht et al. 1995) and ACE-2 (Brenguier et al. 2000). In particular, they can be compared to values quoted by Boucher and Lohmann (1995) of the relationship between sulfate and cloud droplet concentration. Their Figure 1a uses measurements made by Hegg et al. (1993) during ASTEX in the northeast Atlantic Ocean. In the present study, Figure 3 shows, for example, that the sulfate concentration in the lowest 2 km on 2 April was 4 nmol m^{-3} (~0.4 μg m^{-3}) and increased to 25-30 nmol m^{-3} (~2.5 –3.0 μg m^{-3}) on 5 April. The corresponding increase in N_{ad} was from 85 to 300 cm^{-3}; this increase is quantitatively similar to

the model based on the Hegg et al. (1993) measurements. Although the uncertainty in cloud optical depth contributes to uncertainty in cloud droplet number concentration, this uncertainty is small relative to the three- to four-fold change in N_{ad} over the episode, confirming attribution of the changes in effective radius to the Twomey mechanism.

The method presented here to estimate N_{ad} and the vertical extent of the cloud depends quite critically on the location of the cloud base. Remote sensing methods to pin down this elusive parameter would be beneficial. In their analysis of tropical convective clouds, Rosenfeld and Lensky (1998) chose to locate cloud base at a level 2K warmer than the warmest cloud pixel in the region. However, a problem with this approach evident in Figure 4 (a) and (b) is that the identification of the warmest cloud pixel depends on the threshold used. Without additional information, the ability to use this strategy to investigate the effect of industrial aerosol on cloud vertical extent is limited. If systematic differences in cloud thickness arise as a result of changes in cloud microphysics, it will be essential to include these in estimates of the aerosol indirect effect. For instance, in ACE-2 Brenguier et al. (2000) observed a greater geometrical thickness of marine cloud on the low aerosol day. The same is observed in this study, but we cannot ascribe it to a single cause. The smaller geometrical cloud thickness on 5 April occurs in spite of the unstable conditions around the intense low-pressure center.

6. Conclusions

We have used the output of a chemical transport and transformation model to identify a several-day episode in which sulfate aerosol from industrial sources might be expected to exert a strong influence on cloud microphysical and radiative properties in an oceanic area that is well away from source regions. Pertinent cloud microphysical properties (optical depth, cloud drop radius, and cloud drop column concentration) are inferred from radiance data obtained from satellite remote sensing. Comparison of these quantities in situations where the model indicates the presence or absence of industrial sulfate has allowed identification, on a synoptic scale, of the expected signature of one aerosol indirect effect – an increase in droplet number concentration and

concomitant decrease in droplet radius consistent with expectation according to the Twomey indirect forcing mechanism.

We have also been able to estimate the adiabatic cloud droplet number concentration by identifying the cloud base from meteorological analyses and assuming that cloudy pixels represent the tops of air parcels ascending to different levels. The adiabatic cloud droplet number concentration ranged from 65 – 95 cm^{-3} on days when the chemistry model indicated that little sulfate was present, and was 300 cm^{-3} during the peak of the sulfate incursion. Mirroring this difference, it is found that the cloud drop effective radius ranged up to 20 μm on the low-sulfate days but was generally less than 12 μm on the high-sulfate days.

This study demonstrates the ability to use a chemical transport and transformation model to identify situations where the influence of continental sulfate aerosol on cloud microphysical properties may be expected and the ability as well to quantify this influence by remote sensing from satellite. This approach may therefore have widespread applicability in quantifying the indirect effect of anthropogenic aerosols.

Acknowledgments. We thank Jim Coakley for computer code and advice on the use of the spatial coherence method for AVHRR GAC data and Takashi Nakajima of NASDA/EORC, Japan, for providing us with the retrieval module. We also thank two anonymous reviewers for valuable comments. Data to drive the chemical transport model were obtained from ECMWF. This study was partially supported by NASA training grant NGT5-30040 and NASA grant NAG5-7727. Work at BNL was supported also by the Environmental Sciences Division of the U. S. Department of Energy and was performed under Contract No. DE-AC02-98CH10886.

REFERENCES

Ackerman, A.S., O.B. Toon, D.E. Stevens, A.J. Heymsfield, V. Ramanathan, and E.J. Welton, 2000: Reduction of tropical cloudiness by soot. *Science,* **288**, 1042-1047.

Agee, E.M., 1987: Mesoscale cellular convection over the oceans. *Dynamics of Atmospheres and Oceans*, **10**, 317-341.

Albrecht, B.A., 1989: Aerosols, cloud microphysics, and fractional cloudiness. *Science*, **245**, 1227-1230.

_____, C.S. Bretherton, D. Johnson, W.H. Schubert, and A.S. Frisch, 1995: The Atlantic Stratocumulus Transition Experiment – ASTEX. *Bull. Amer. Meteor. Soc.,* **76,** 889-904.

Bader, M.J., G.S. Forbes, J.R. Grant, R.B.E. Lilley, and A.J. Waters, 1995: Images in weather forecasting: A practical guide for interpreting satellite and radar imagery. *Cambridge University Press*, 499 pp.

Benkovitz, C.M., and S.E. Schwartz, 1997: Evaluation of modeled sulfate and SO_2 over North America and Europe for four seasonal months in 1986-87. *J. Geophys. Res.*, **102**, 25,305-25,338.

_____, C.M. Berkowitz, R.C. Easter, S. Nemesure, R. Wagener, and S.E. Schwartz, 1994: Sulfate over the North Atlantic and adjacent continental regions: Evaluation for October and November 1986 using a three-dimensional model driven by observation-derived meteorology. *J. Geophys. Res.,* **99**, 20,725-20,756.

_____, M.A. Miller, S.E. Schwartz, O.-U. Kwon, 2001a: The influence of cut-off lows on sulfate burdens over the North Atlantic during April, 1987. Preprints, *A Millennium Symposium on Atmospheric Chemistry*, Albuquerque, NM, Amer. Meteor. Soc., 170-174.

_____, M.A. Miller, S.E. Schwartz, O.-U. Kwon, 2001b: Dynamical influences on the distribution and loading of SO_2 and sulfate over North America, the North Atlantic and Europe in April 1987. *Geochem. Geophys. Geosys., (G3),* **2**, 2000GC000129.

Boucher, O., and U. Lohmann, 1995: The sulfate – CCN-cloud albedo effect: A sensitivity study with two general circulation models. *Tellus*, **47B**, 281-300.

Brenguier, J.-L., H. Pawlowska, L. Schüller, R. Preusker, J. Fischer, and Y. Fouquart, 2000: Radiative properties of boundary layer clouds: Droplet effective radius versus number concentration. *J. Atmos. Sci.,* **57**, 803-821.

Cahalan, R.F., W. Ridgway, W.J. Wiscombe, T.L. Bell, and J.B. Snider, 1994: The albedo of fractal stratocumulus clouds. *J. Atmos. Sci.,* **51**, 2434-2455.

Coakley, J.A., Jr., and F.P. Bretherton, 1982: Cloud cover from high-resolution scanner data: Detecting and allowing for partially filled fields of view. *J. Geophys. Res*., **87**, 4917-4932.

_____, and R. Davies, 1986: The effect of cloud sides on reflected solar radiation as deduced from satellite observations. *J. Atmos. Sci.*, **43**, 1025-1035.

Han, Q., W.B. Rossow, and A.A. Lacis, 1994: Near-global survey of effective droplet radii in liquid water clouds using ISCCP data. *J. Climate*, **7**, 465-497.

_____, W.B. Rossow, J. Chou, and R.M. Welch, 1998: Global variation of column droplet concentration in low-level clouds. *Geophys. Res. Lett.,* **25**, 1419-1422.

Hansen, J.E., and L.D. Travis, 1974: Light scattering in planetary atmospheres. *Space Sci. Rev*., **16**, 527-610.

_____, M. Sato, and R. Ruedy, 1997: Radiative forcing and climate response. *J. Geophys. Res*., **102**, 6831-6864

Haywood, J., and O. Boucher, 2000: Estimates of the direct and indirect radiative forcing due to tropospheric aerosols: A review. *Rev. Geophys*. **38**, 513-543.

Hegg, D.A., R.J. Ferek, and P.V. Hobbs, 1993: Light scattering and cloud condensation nucleus activity of sulfate aerosol measured over the northeast Atlantic Ocean. *J. Geophys. Res.*, **98**, 14,887-14,894.

Kaufman, Y.J., and T. Nakajima, 1993: Effect of Amazon smoke on cloud microphysics and albedo – analysis from satellite imagery. *J. Appl. Meteor*., **32**, 729-744.

_____, and B.N. Holben, 1993: Calibration of the AVHRR visible and near-IR bands by atmospheric scattering, ocean glint and desert reflection. *Int. J. Remote Sens*., **14**, 21-52.

King, M.D., 1987: Determination of the scaled optical thickness of clouds from reflected solar radiation measurements. *J. Atmos. Sci*., **44**, 1734-1751.

Loeb, N.G., and J.A. Coakley, Jr., 1998: Inference of marine stratus cloud optical depths from satellite measurements: Does 1D theory apply? *J. Climate*, **11**, 215-233.

Lohmann, U., G. Tselioudis, and C. Tyler, 2000: What causes the difference in relationship of cloud optical depth with cloud droplet effective radius for optically thin and thick clouds? *Geophys. Res. Lettr.,* **27**, 1099-1102.

Martin, G.M., D.W. Johnson, and A. Spice, 1994: The measurement and parameterization of effective radius of droplets in warm stratocumulus clouds. *J. Atmos. Sci*., **51**, 1823-1842.

Nakajima, T, and M.D. King, 1990: Determination of the optical thickness and effective particle radius of clouds from reflected solar radiation measurements. Part I: Theory. *J. Atmos. Sci*., **47**, 1878-1893.

_____, M.D. King, J. Spinhirne, and L. Radke, 1991: Determination of the optical thickness and effective particle radius of clouds from reflected radiation measurements. Part II: Marine stratocumulus observations. *J. Atmos. Sci.*, **48**, 728-750.

Nakajima, T.Y., and T. Nakajima, 1995: Wide-area determination of cloud microphysical properties from NOAA AVHRR measurements for FIRE and ASTEX regions. *J. Atmos. Sci*., **52**, 4043-4059.

Platnick, S., and F.P.J. Valero, 1995: A validation of a satellite cloud retrieval during ASTEX. *J. Atmos. Sci.,* **52**, 2985-3001.

Radke, L.F., J.A. Coakley, Jr., and M.D. King, 1989: Direct and remote sensing observations of the effects of ships on clouds. *Science*, **246**, 1146-1149.

Rosenfeld, D., and I.M. Lensky, 1998: Satellite-based insights into precipitation formation processes in continental and maritime convective clouds. *Bull. Amer. Meteor. Soc.,* **79,** 2457-2476.

Reynolds, R.W., 1988: A real-time global sea surface temperature analysis. *J. Climate*, **1**, 75-86.

Schwartz, S.E., and A. Slingo, 1996: Enhanced shortwave cloud radiative forcing due to anthropogenic aerosols. *Clouds, Chemistry and Climate – Proceedings of NATO Advanced Research Workshop*, P. Crutzen and V. Ramanathan, Ed., Springer, 191-236.

Shine, K.P., Y. Fouquart, V. Ramaswamy, S. Solomon, and J. Srinivasan, 1995: Radiative Forcing. *Climate Change 1994: Radiative Forcing of Climate Change,* J.T. Houghton et al., Ed., Cambridge University Press, 163-203.

Stephens, G.L., 1984: The parameterization of radiation for numerical weather prediction and climate models. *Mon. Wea. Rev*., **112**, 826-867.

Trenberth, K.E., 1992: Global analyses from ECMWF and atlas of 1000 mb to 10mb circulation statistics. NCAR Technical Note, NCAR/TN-373+STR, 191 pp.

Twomey, S., 1977: The influence of pollution on the short-wave albedo of clouds. *J. Atmos. Sci.*, **34**, 1149-1152.

_____, and C.F. Bohren, 1980: Simple approximations for calculations of absorption in clouds. *J. Atmos. Sci.,* **37**, 2086-2094.

Wetzel, M.A., and L.L. Stowe, 1999: Satellite-observed patterns in stratus microphysics, aerosol optical thickness, and shortwave radiative forcing. *J. Geophys. Res*., **104**, 31 287-31 229.

Figure Captions

1. Channel 1 (0.58 – 0.68 μm) AVHRR images of the eastern North Atlantic Ocean at dates and times indicated. The study area is bounded by latitudes 50 and 55N and longitudes 25 and 30W.
2. As in Figure 1 but for Channel 4 (10.3 – 11.3μm).
3. Model simulations of the vertical profiles of the sulfate concentration (nmol m^{-3}) averaged over 50-55N and 25-30W at 1200 UTC on the dates marked.
4. (a) Scatter plot of AVHRR Channel 1 reflectance (%) and Channel 4 radiating temperature (K) on 2 April 1987 for the region bounded by latitudes 50 and 55N and longitudes 25 and 30W; (b) scatter plot of Channel 4 local standard deviation (mW m^{-2} sr^{-1} cm) for the same region and time period.
5. (a) Retrieved cloud optical depth for all pixels in Figure 3(a) having reflectance in excess of 10% plotted versus the inferred cloud top temperature; (b) the subset of pixels in (a) that also have Channel 4 local standard deviation less than 0.5 mW m^{-2} sr^{-1} cm.
6. Retrieved cloud droplet effective radius, r_e (μm), plotted versus the inferred cloud top temperature in the study region at dates and times indicated.
7. Retrieved effective cloud droplet radius, r_e (μm), plotted versus the cloud optical depth at 0.64 μm in the study region at dates and times indicated.
8. Inferred column droplet concentration, C (10^6 cm^{-2}), plotted versus the inferred cloud top temperature in the study region at dates and times indicated. Superimposed on each scatter plot is an estimate of the adiabatic value of C for the cloud base obtained from meteorological analyses and for the adiabatic cloud droplet number concentration, N_{ad} (cm^{-3}) marked on the panels.

TABLE 1. Remote sensing parameters, sulfate burden and cloud properties during the study period.

Date April 1987	Time UTC	Solar Zenith Angle (deg)	Satellite View Angle (deg)	Relative azimuth Angle (deg)	Sulfate Column Burden (μmol m^{-2}) at 1200 UTC	Cloud Base at 1200 UTC		Cloud Top at 1200 UTC		Adiabatic Cloud Droplet Concentration (cm^{-3})
						Temperature (K)	Altitude (m)	Temperature (K)	Altitude (m)	
2	1628	58	20	150	25	271.0	1400	262.5	2710	85
3	1617	56	8	150	17	273.0	910	263.0	2450	95
4	1606	55	4	30	84	274.5	880	268.0	1880	230
5	1555	54	15	32	115	276.0	530	270.0	1460	300
6	1544	52	25	32	85	275.0	820	267.0	2050	190
7	1534	51	34	33	70	274.2	690	263.0	2420	120
8	1524	50	38	33	23	274.5	430	262.0	2350	65
8	1705	60	44	154	23	274.5	430	262.0	2350	90

Sulfate column burden is an average for area 50 – 55N, 25 – 30W, as shown in Figure 1. Remote sensing parameters are for the center of that grid cell. Relative azimuth (column 5) is defined such that 0° is forward scattering and 180° is the backscattering direction.

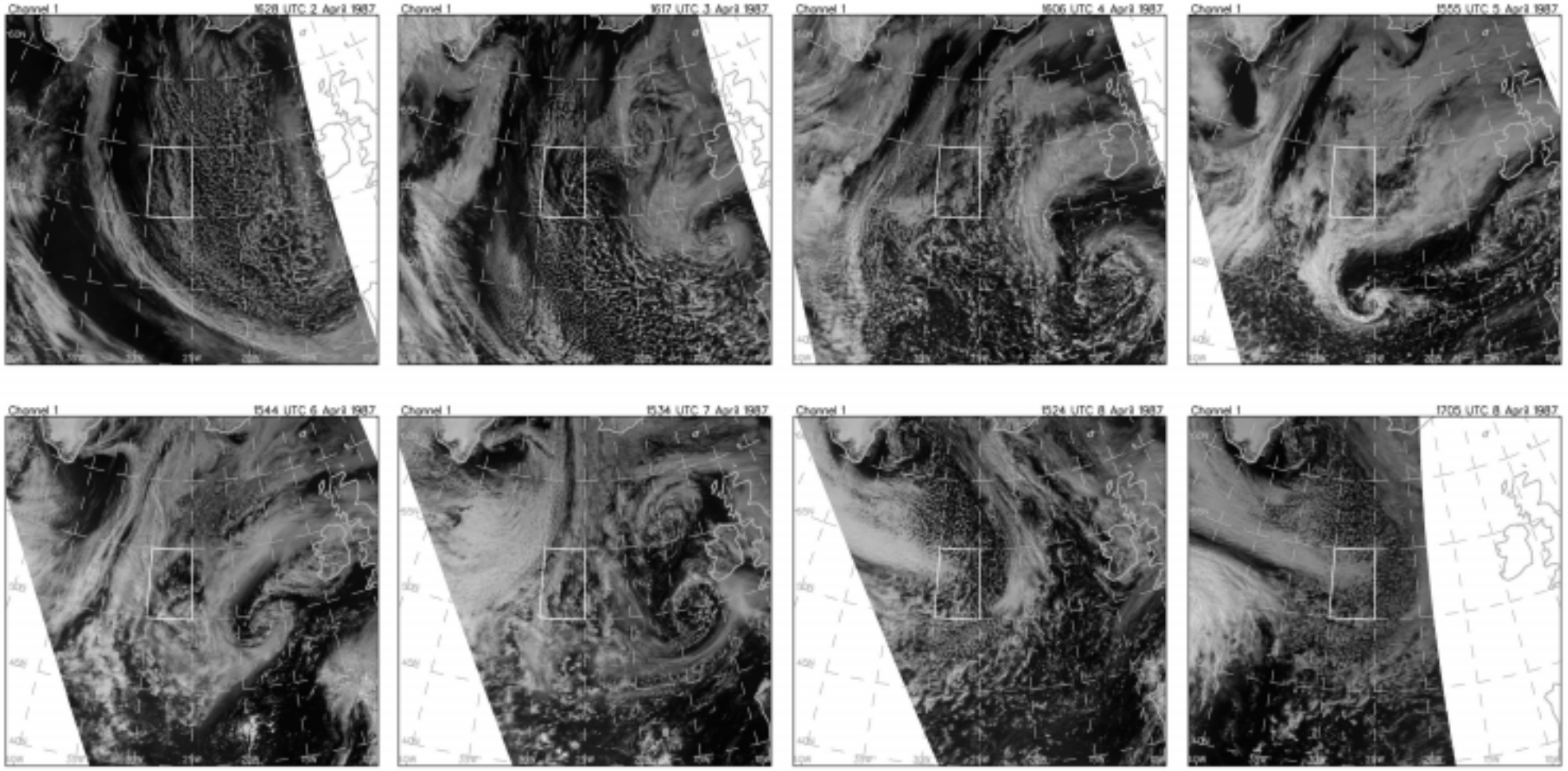
Channel 1
1628 UTC 2 April 1987
Channel 1
1617 UTC 3 April 1987
Channel 1
1606 UTC 4 April 1987
Channel 1
1555 UTC 5 April 1987
Channel 1
1544 UTC 6 April 1987
Channel 1
1534 UTC 7 April 1987
Channel 1
1524 UTC 8 April 1987
Channel 1
1705 UTC 8 April 1987

Figure 1

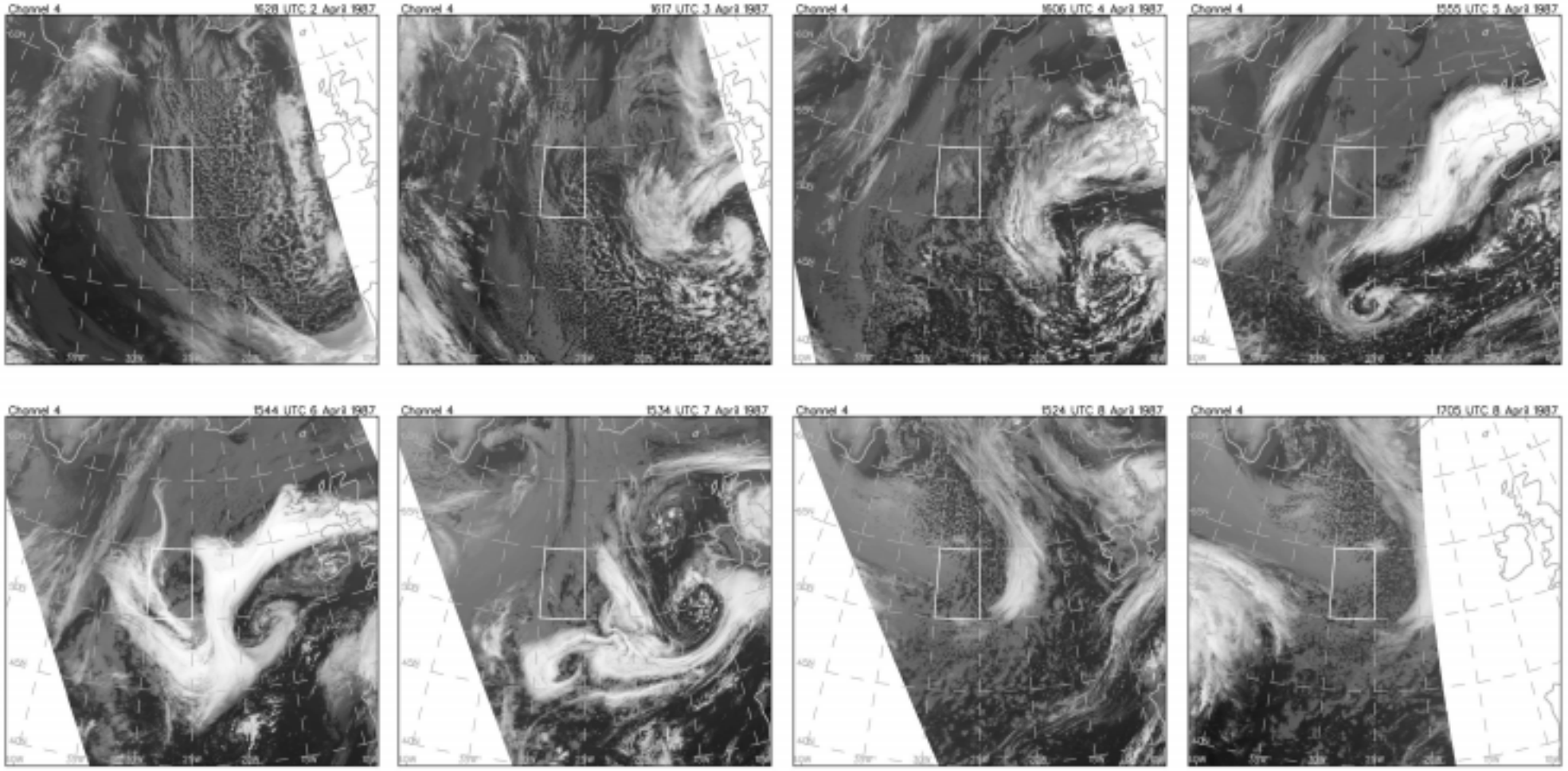
Channel 4
1628 UTC 2 April 1987
Channel 4
1617 UTC 3 April 1987
Channel 4
1606 UTC 4 April 1987
Channel 4
1555 UTC 5 April 1987
Channel 4
1544 UTC 6 April 1987
Channel 4
1534 UTC 7 April 1987
Channel 4
1524 UTC 8 April 1987
Channel 4
1705 UTC 8 April 1987

Figure 2

Figure 3

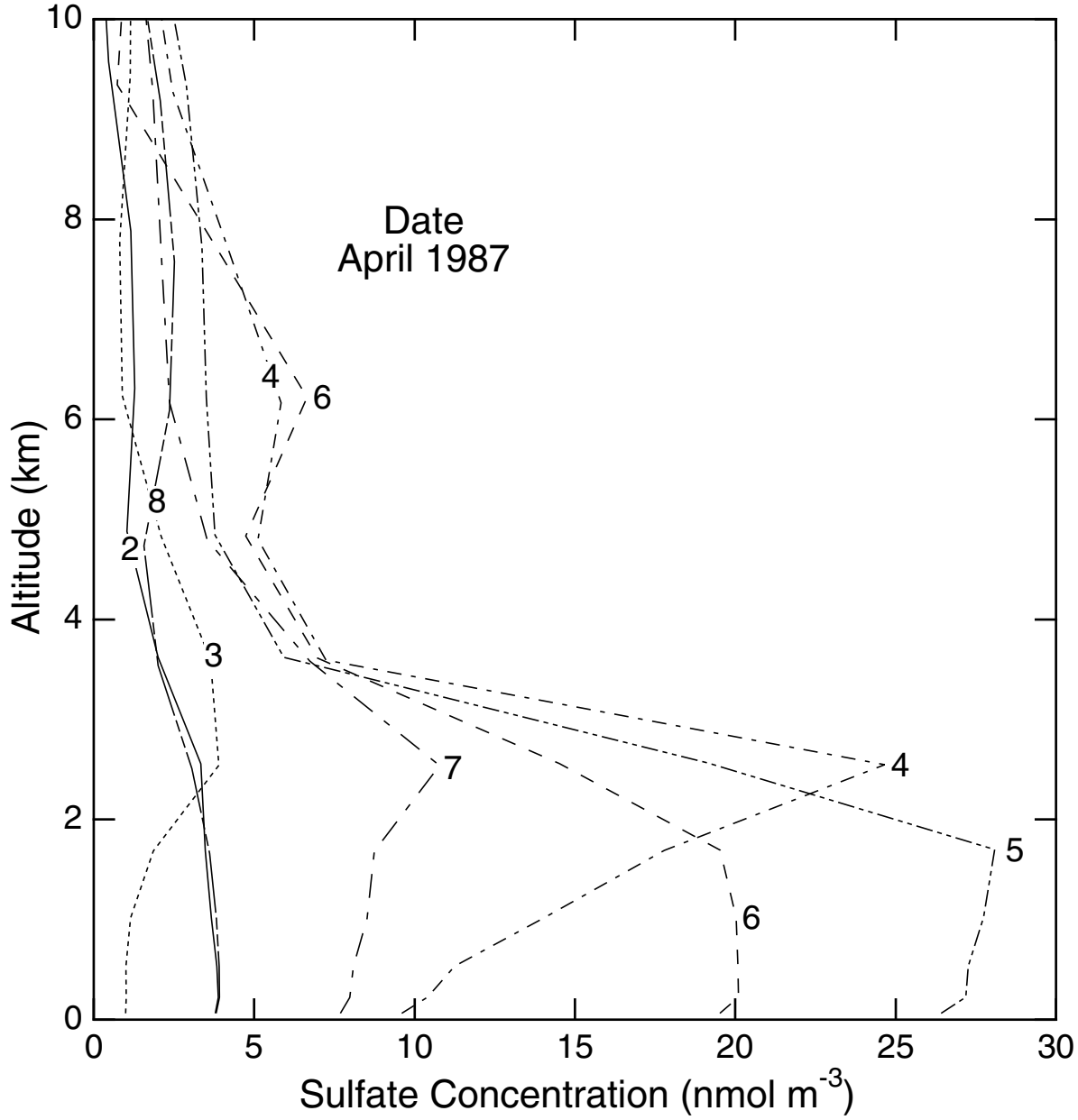
Date
April 1987
Altitude (km)
Sulfate Concentration (nmol m-3)
0
2
4
6
8
10
0
5
10
15
20
25
30
4
6
8
2
3
7
4
5
6

Figure 4

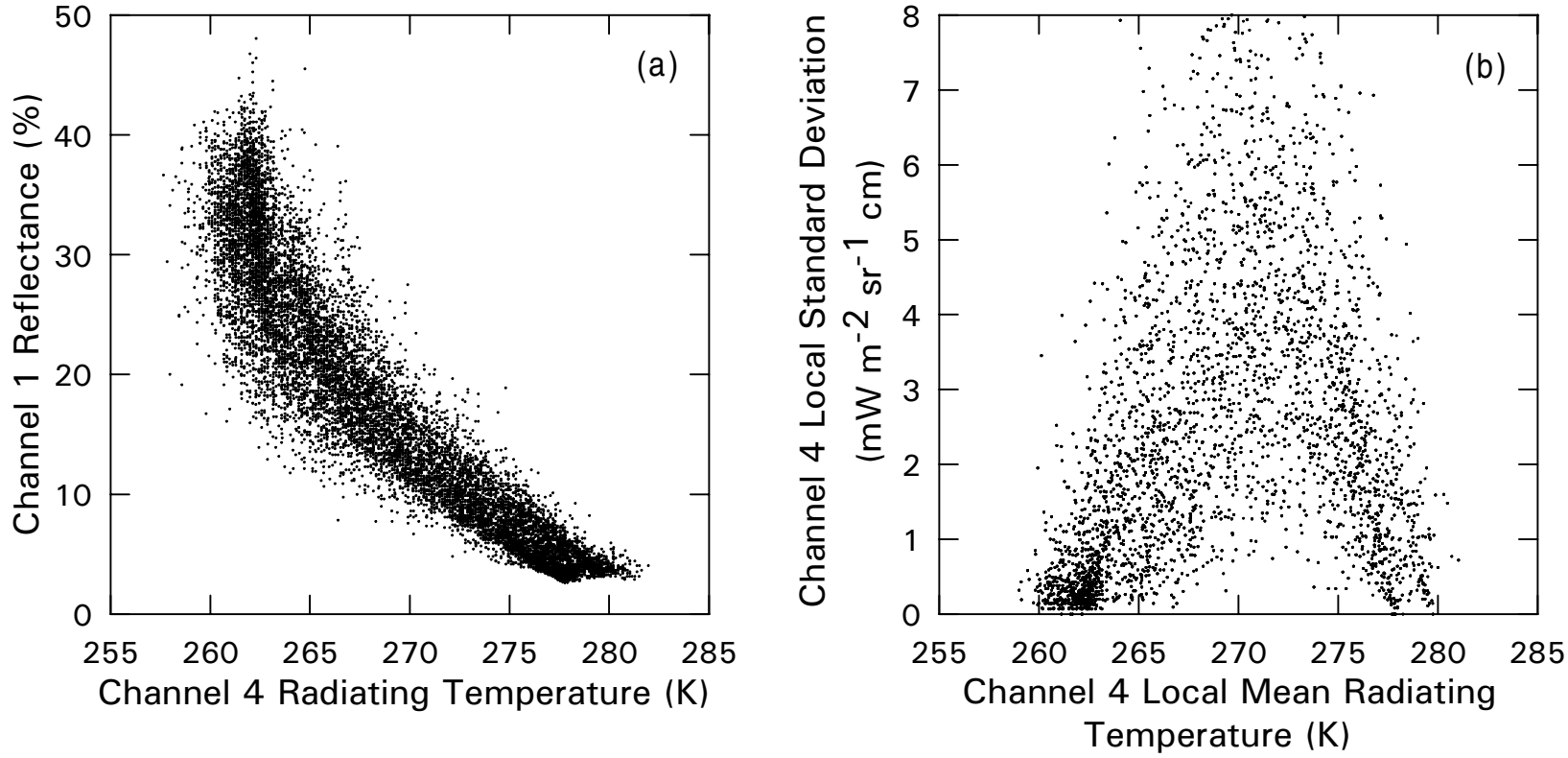
(a)
Channel 1 Reflectance (%)
0
10
20
30
40
50
255
260
265
270
275
280
285
Channel 4 Radiating Temperature (K)
(b)
Channel 4 Local Standard Deviation
(mW m-2 sr-1 cm)
0
1
2
3
4
5
6
7
8
255
260
265
270
275
280
285
Channel 4 Local Mean Radiating
Temperature (K)

Figure 5

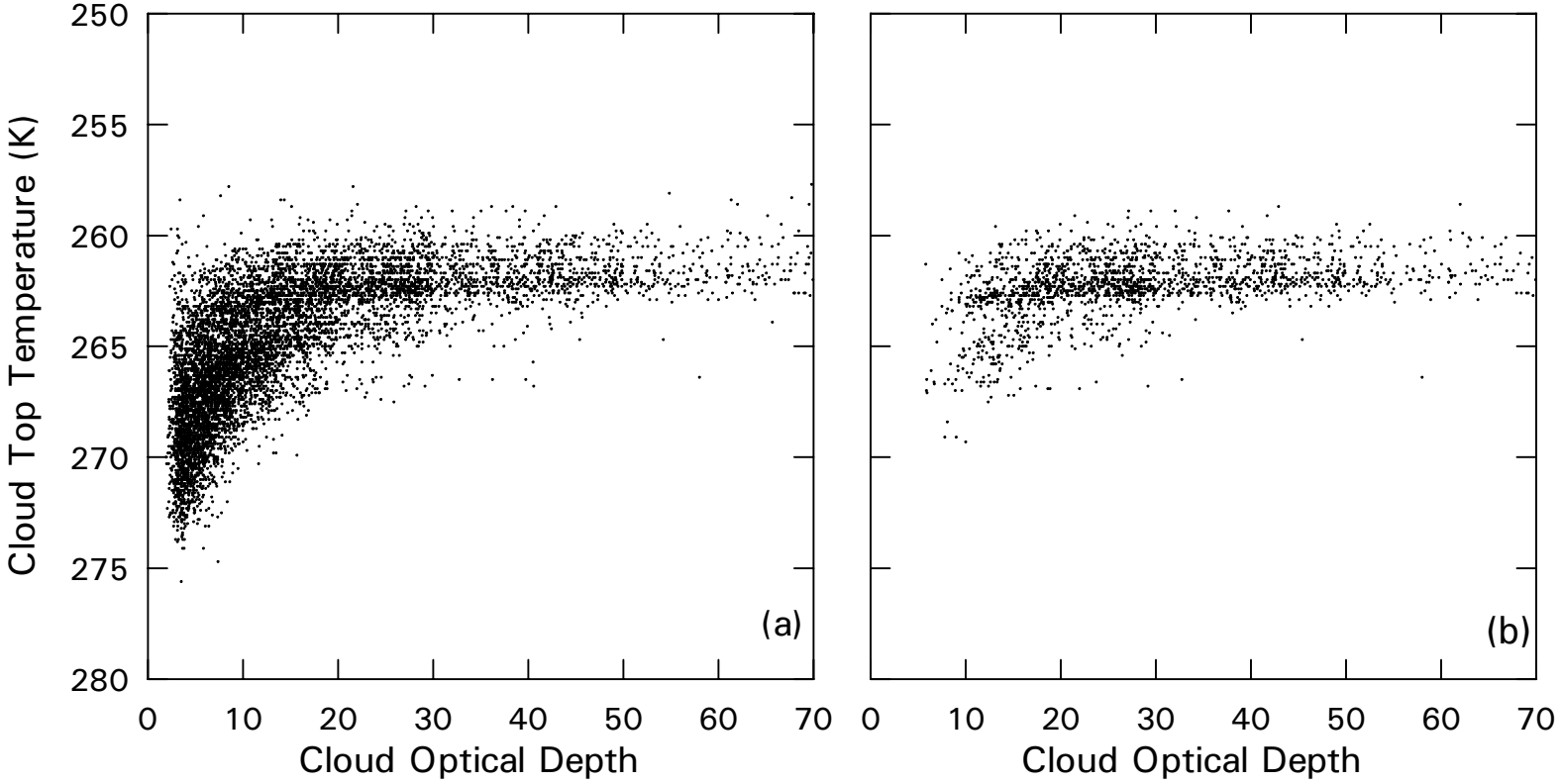
Cloud Top Temperature (K)
250
255
260
265
270
275
280
0
10
20
30
40
50
60
70
Cloud Optical Depth
(a)
(b)

Figure 6

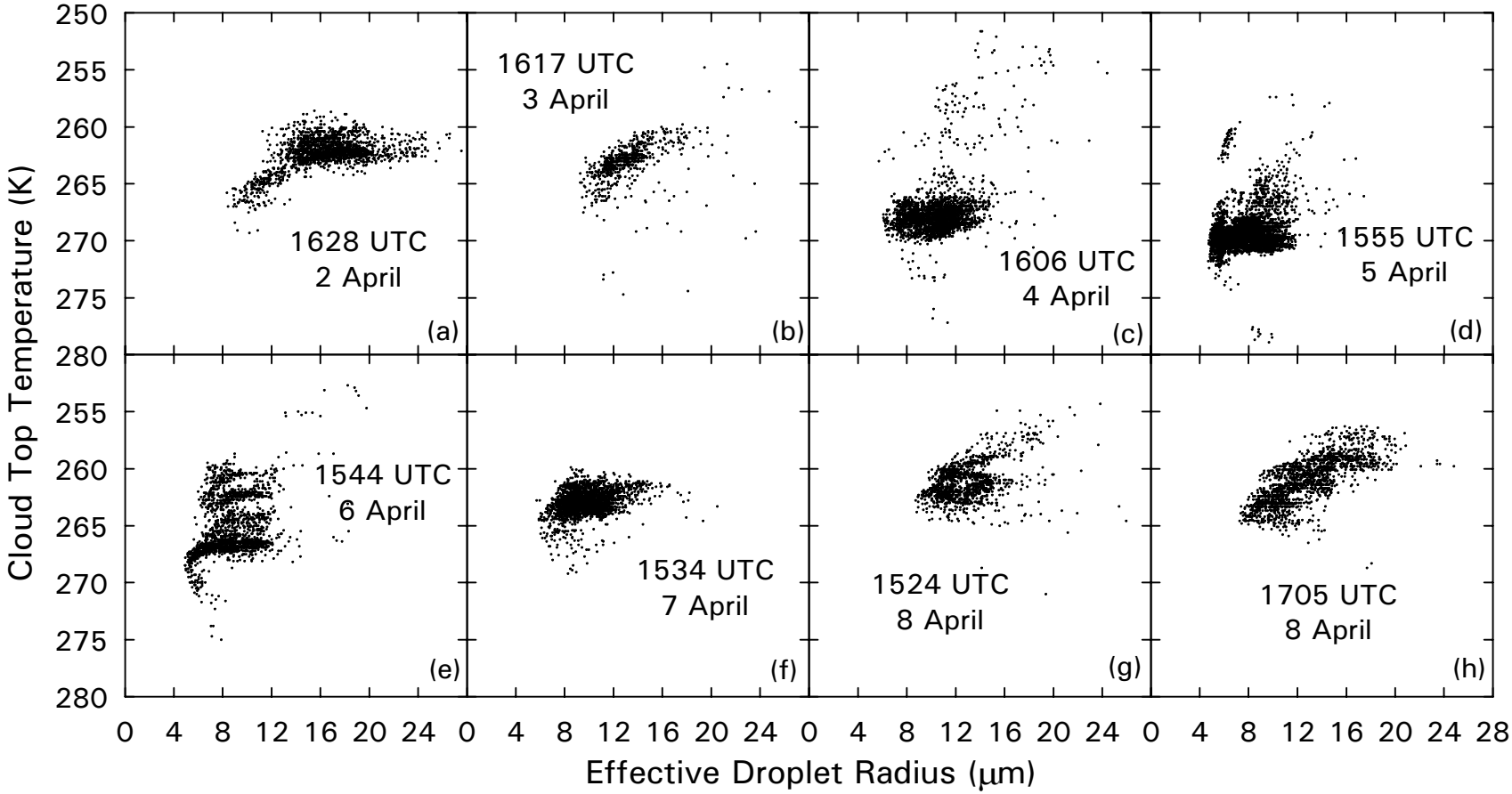
Cloud Top Temperature (K)
250
255
260
265
270
275
280
1628 UTC
2 April
(a)
1617 UTC
3 April
(b)
1606 UTC
4 April
(c)
1555 UTC
5 April
(d)
1544 UTC
6 April
(e)
1534 UTC
7 April
(f)
1524 UTC
8 April
(g)
1705 UTC
8 April
(h)
0 4 8 12 16 20 24 0 4 8 12 16 20 24 0 4 8 12 16 20 24 0 4 8 12 16 20 24 28
Effective Droplet Radius (μm)

Figure 7

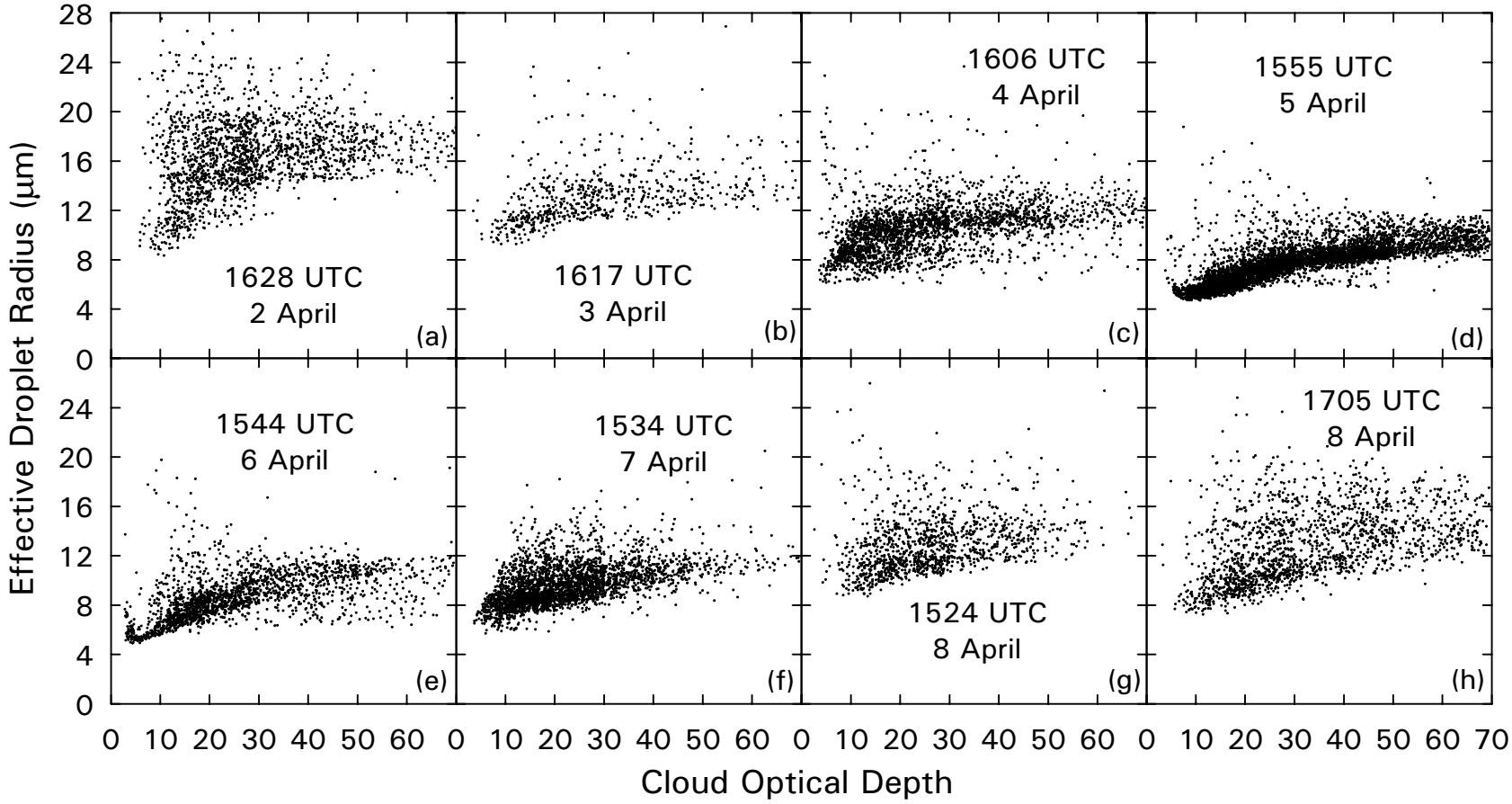
Effective Droplet Radius (μm)
Cloud Optical Depth
1628 UTC
2 April
(a)
1617 UTC
3 April
(b)
1606 UTC
4 April
(c)
1555 UTC
5 April
(d)
1544 UTC
6 April
(e)
1534 UTC
7 April
(f)
1524 UTC
8 April
(g)
1705 UTC
8 April
(h)

Figure 8

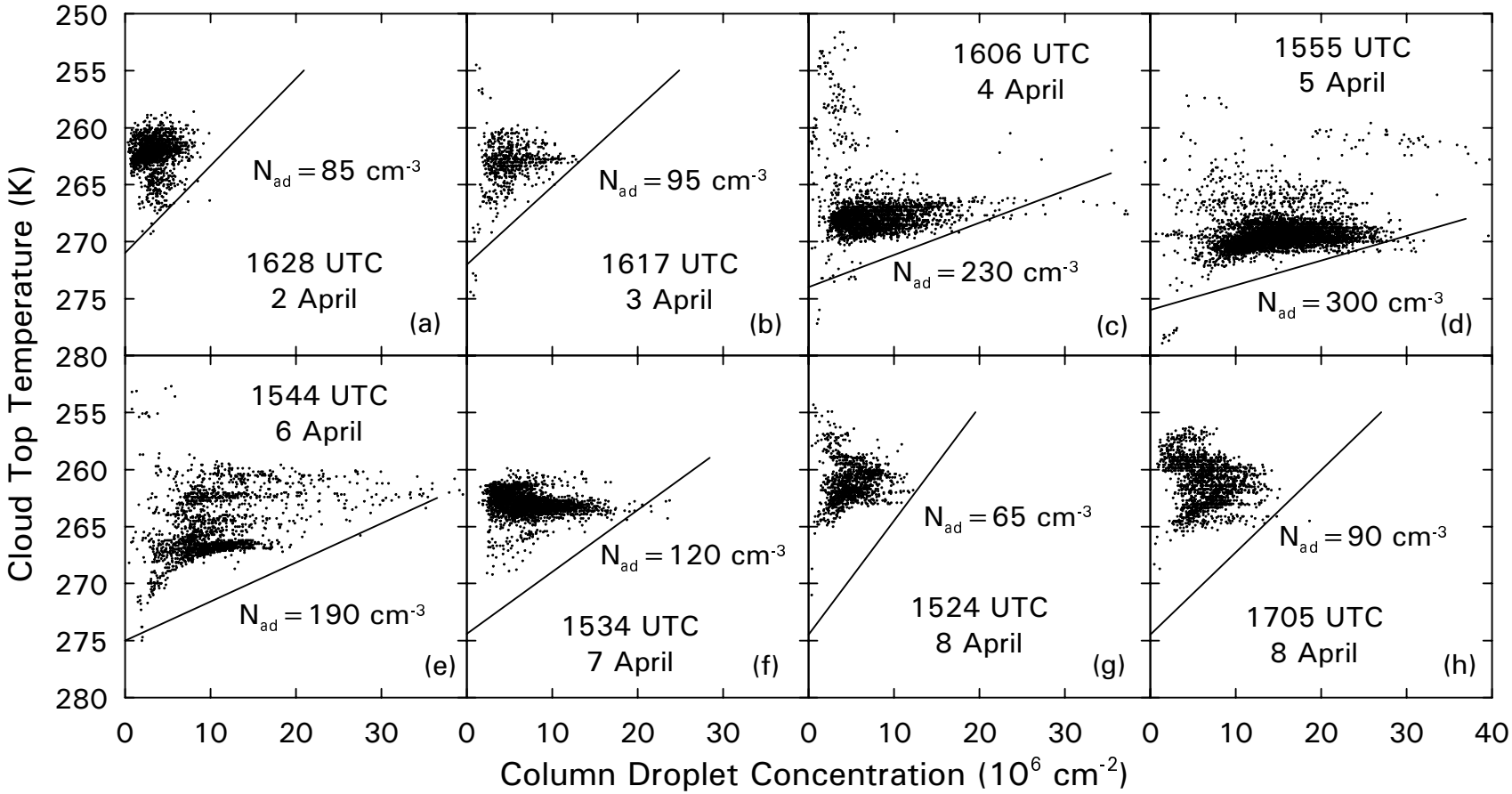
Cloud Top Temperature (K)
Column Droplet Concentration (10^6 cm^{-2})
N_{ad} = 85 cm^{-3}
1628 UTC
2 April
(a)
N_{ad} = 95 cm^{-3}
1617 UTC
3 April
(b)
1606 UTC
4 April
N_{ad} = 230 cm^{-3}
(c)
1555 UTC
5 April
N_{ad} = 300 cm^{-3}
(d)
1544 UTC
6 April
N_{ad} = 190 cm^{-3}
(e)
N_{ad} = 120 cm^{-3}
1534 UTC
7 April
(f)
N_{ad} = 65 cm^{-3}
1524 UTC
8 April
(g)
N_{ad} = 90 cm^{-3}
1705 UTC
8 April
(h)